PHYSICAL REVIEW B **102**, 165425 (2020)

Transport study of the wormhole effect in three-dimensional topological insulators

Ming Gong,[1] Ming Lu,[2,1] Haiwen Liu,[3] Hua Jiang,[4,5,*] Qing-Feng Sun,[1,6,7] and X. C. Xie[1,2,7,†]
[1]*International Center for Quantum Materials, School of Physics, Peking University, Beijing 100871, China*
[2]*Beijing Academy of Quantum Information Sciences, West Bld.3, No.10 Xibeiwang East Rd., Haidian District, Beijing 100193, China*
[3]*Center for Advanced Quantum Studies, Department of Physics, Beijing Normal University, Beijing 100875, China*
[4]*School of Physical Science and Technology, Soochow University, Suzhou 215006, China*
[5]*Institute for Advanced Study and School of Physical Science and Technology, Soochow University, Suzhou 215006, China*
[6]*Collaborative Innovation Center of Quantum Matter, Beijing 100871, China*
[7]*CAS Center for Excellence in Topological Quantum Computation, University of Chinese Academy of Sciences, Beijing 100190, China*

(Received 27 May 2020; accepted 13 October 2020; published 27 October 2020)

Inside a three-dimensional strong topological insulator, a tube with $h/2e$ magnetic flux carries a pair of protected one-dimensional linear fermionic modes. This phenomenon is known as the "wormhole effect." In this work, we find that the wormhole effect, as a unique degree of freedom, introduces exotic transport phenomena and thus manipulates the transport properties of topological insulators. Our numerical results demonstrate that the transport properties of a double-wormhole system can be manipulated by the wormhole interference. Specifically, the conductance and local density of states both oscillate with the Fermi energy due to the interference between the wormholes. Furthermore, by studying the multiwormhole systems, we find that the number of wormholes can also modulate the differential conductance through a $\mathbb{Z}_2$ mechanism. Finally, we propose two types of topological devices in real applications, the "wormhole switch" device and the "traversable wormhole" device, which can be finely tuned by controlling the wormhole degree of freedom.

DOI: 10.1103/PhysRevB.102.165425

I. INTRODUCTION

Ever since their discovery, topological insulators (TIs) have provided versatile platforms for physicists and material scientists to investigate nontrivial properties of the matter [1,2]. A three-dimensional (3D) TI is a band insulator inside the bulk but carries metallic surface states protected by the time-reversal symmetry [3–8]. The existence of these nontrivial surface states makes TIs ideal candidates for designing low-dissipation electronic devices. Recently, novel physical properties of the surface states have intrigued great interests among physicists. Especially, theoretical studies demonstrated that there is no gapless surface state in a TI nanowire because of the spin-momentum locking induced π Berry phase [9,10]. By applying a π (in units of $\hbar/e$) magnetic flux, the effect of the π Berry phase is eliminated, making the spectrum of the surface states gapless again. Furthermore, an h/e period Aharonov-Bohm oscillation of the magnetoconductance was observed in different TI nanowires [11–15].

Interestingly, a flux tube inside the TI bulk shows the same energy spectrum as the TI nanowire [16]. The π-flux tube carries a pair of gapless linear modes, providing a conducting channel for electrons to tunnel between the opposite surfaces of the TI. Thus, the surface electrons that are spatially separated far away can be connected by such a conducting flux tube. This phenomenon is called the "wormhole effect" and the conducting flux tube is named as the "wormhole" [17], for it acts like a wormhole in general relativity that bridges surfaces separated by an insulating bulk. Previously, by varying the magnetic flux ϕ, numerical studies revealed the existence of the π-flux wormhole and its evolution [16,17]. Such a ϕ-dependence nature inspires us to study the exotic transport phenomena and the corresponding topological device applications based on the wormhole effect. However, systematic transport simulations of the wormhole systems were not yet performed. The main difficulty is that the existing numerical methods rely on the diagonalization of the 3D bulk Hamiltonian, which severely reduces the computation speed and limits studies to very small systems only [16,17]. For this reason, we study the transport properties of the wormhole system in a different approach to overcome the difficulty caused by the bulk Hamiltonian.

In this paper, we construct the model of the wormhole system based on a two-dimensional (2D) effective lattice Hamiltonian (2DELH) for the surface of 3D strong TI, and study the transport properties of the system. This 2DELH captures the key physical properties of the topologically protected surface states without any reference to the bulk Hamiltonian. Therefore, it improves the computational speed significantly and makes it possible to study larger size and more complicated TI systems, especially the wormhole systems. Then, the transport properties of the wormhole system are investigated systematically based on the nonequilibrium Green's function method [18]. Our numerical results of the wormhole systems under different conditions demonstrate that the "wormhole effect," as a unique degree of freedom, brings exotic transport phenomena and makes it feasible to manipulate the transport properties of TIs. By studying a double-wormhole system, we find the differential conductance and the local density of states (LDOS) oscillate with the Fermi energy due to interference

---

[*] jianghuaphy@suda.edu.cn
[†] xcxie@pku.edu.cn

between the wormholes. Therefore, the transport properties of TIs can be manipulated through the wormhole interference. Then, in multiwormhole systems, we find that the number of wormholes can also modulate the differential conductance. These phenomena can be explained by an interwormhole backscattering mechanism. Particularly, in the perspective of transport, this interwormhole backscattering mechanism can be directly related to the $\mathbb{Z}_2$ classification in TIs. In applications, we propose two topological devices that are highly tunable by controlling the wormhole degree of freedom. One is the "wormhole switch" device, where the conducting and insulating status of the device can be switched by varying the magnetic flux among the wormholes. The other is the "traversable wormhole" device, in which a pair of conducting wormholes serves as a bridge that connects isolated regions, and enables electrons to travel between them.

This paper is organized as follows. In Sec. II, we introduce the 2DELH for the wormhole systems and the numerical methods to calculate the transport observables. In Sec. III, we investigate the interfering transport between wormholes for the double-wormhole and the multiwormhole systems. In Sec. IV, we propose two topological device applications based on the wormhole systems. Finally, we conclude the paper with a perspective in Sec. V.

II. MODEL AND METHODS

A. Surface Hamiltonian and 2D lattice model of the wormhole system

We construct the lattice model for the wormhole system based on the 2DELH, which incorporates a so-called Wilson mass term to overcome the fermion-doubling problem [19–24].[1] The low-energy effective Hamiltonian of this model is

$$H(\mathbf{k}) = \hbar v_F(\hat{\sigma}\times\mathbf{k})\cdot\hat{n} + \frac{Wa}{2}k_n^2\sigma_z, \tag{1}$$

where v_F is the Fermi velocity of the topological surface states and $\hat{\sigma}\equiv(\sigma_x,\sigma_y,\sigma_z)$ with $\sigma_{x,y,z}$ the Pauli matrices, $\mathbf{k}=(k_x,k_y,k_z)$ is the wave vector, and $\hat{n}$ is the outward normal vector of the surface. The second term in $H(\mathbf{k})$ is the Wilson mass term and k_n is the component of the wave vector perpendicular to $\hat{n}$ direction. In the x-y plane, the discretized 2D square-lattice Hamiltonian is written as

$$\begin{aligned} H_{2\mathrm{D}} = {}& \sum_{\mathbf{i}}\frac{i\hbar v_F}{2a}\left(c_{\mathbf{i}}^{\dagger}\sigma_y c_{\mathbf{i}+\delta\hat{\mathbf{x}}} - c_{\mathbf{i}}^{\dagger}\sigma_x c_{\mathbf{i}+\delta\hat{\mathbf{y}}}\right) \\ & -\sum_{\mathbf{i}}\frac{W}{2a}\left(c_{\mathbf{i}}^{\dagger}\sigma_z c_{\mathbf{i}+\delta\hat{\mathbf{x}}} + c_{\mathbf{i}}^{\dagger}\sigma_z c_{\mathbf{i}+\delta\hat{\mathbf{y}}}\right) + \mathrm{H.c.} \\ & +\sum_{\mathbf{i}}\frac{2W}{a}c_{\mathbf{i}}^{\dagger}\sigma_z c_{\mathbf{i}}, \end{aligned} \tag{2}$$

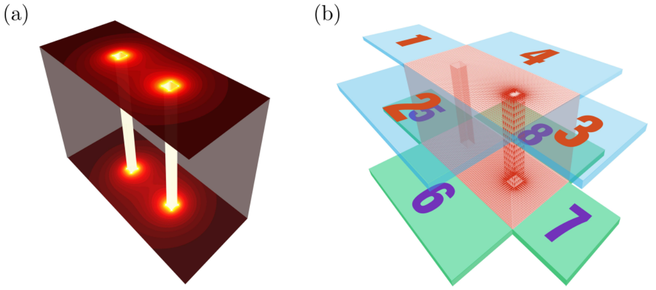

FIG. 1. (a) Sketch of a double-wormhole system. Here, the flux tubes (with light color) inside the TI bulk represent the wormholes. (b) Schematic diagram of the studied multiterminal device. Each terminal contact with the double-wormhole central region is considered as a source or drain. Electrons can transport between these terminals.

where $c_{\mathbf{i}}$ and $c_{\mathbf{i}}^{\dagger}$ are the annihilation and creation operators on site $\mathbf{i}$. $\delta\hat{\mathbf{x}}$ ($\delta\hat{\mathbf{y}}$) is the primitive vector of the square lattice along the x (y) direction, and a is the lattice constant. Although the incorporation of the Wilson mass term successfully overcomes the Fermi-doubling problem by opening a gap at the redundant Dirac cones, it slightly shifts the Berry phase of the eigenstates $\psi_{\pm}(\mathbf{k})$ around the Fermi surface from $\gamma_{\pm}=\pi$ to $\gamma_{\pm}=\pi(1\pm\frac{Wa}{2\hbar v_F}k_F)\approx\pi(1\pm\frac{Wa}{2(\hbar v_F)^2}E_F)$ [19,25]. For this reason, the Fermi energy E_F cannot be too large to hold the π Berry phase. In this paper, we take $a=1$, $\hbar v_F=1$, and $W=0.3$. Under this condition, the relative error in the Berry phase will be smaller than 3% in the energy range $-0.2 < E_F < 0.2$. In order to include the magnetic flux, an additional phase factor $e^{i\phi_{ij}}$ is multiplied to the hopping term in Eq. (2). The summation of ϕ_{ij} along any closed loop, both around the wormhole and the surface, equals to the total magnetic flux inside it [26]. With the help of Eq. (1) or (2), we can study the topological surface states determined by the 3D Hamiltonian within the 2D frame [7], thus can greatly enhance the computational efficiency.[2]

Nevertheless, it is far from enough to construct the Hamiltonian of the wormhole system with Eq. (1) or (2) only. From Fig. 1, the studied system should include the wormhole surfaces and the top and bottom surfaces of the topological insulator. As has widely been discussed [16,27–31], the low-energy effective Hamiltonian with the form like Eq. (1) only works on a flat surface. On a curved surface (e.g., see Fig. 1), the curvature enters the Hamiltonian through the non-Abelian spin connection. Thus, the discretized lattice Hamiltonian can no longer be written in a concise form as Eq. (2). To solve such a problem, we propose a simple method in Appendix A to

---

[1] The natural crystallographic lattices such as the 3D TIs have no fermion-doubling problem. However, the transport properties of the TIs are dominant by the 2D topological surface states. The 2D topological surface states cannot be viewed as a realistic 2D system because they only exist in the presence of the 3D topological nontrivial bulk.

[2] In calculations, the utilization of the 2D lattice model greatly improves the calculating efficiency compared to directly diagonalize the 3D bulk Hamiltonian. For simplicity, suppose that the geometrical size of a 3D system is N^3. The 2D model Hamiltonian reduces the systems size by N and the lattice sites that should be considered are $\propto N^2$. Therefore, the computation speed for standard diagonalization operations is improved by $O(N^3)$.

deal with the discretized 2D Dirac Hamiltonian on the curved surface. The spirit of this method is dividing the whole surface of the wormhole system into a set of flat surfaces, on which the 2D Dirac Hamiltonians have the form of Eq. (1) or (2). Then, the surface of the wormhole system is reconstructed by gluing these flat surfaces together through unitary transformations on a locally defined spinor basis as matching conditions. The necessity of including these matching conditions is rooted from the spin-momentum locking nature of the topological surface states (for example, it is unnecessary to introduce the matching condition when constructing a lattice Hamiltonian with the same geometry for ordinary electron gas without spin-orbit coupling). It correlates the spatial motions and spin rotations of electrons. In our model, the curvature effects emerge when electrons move around the corner that connects the top and bottom surfaces and the wormhole side surfaces. The validity of the 2DELH is verified in Appendix B by investigating the single-wormhole system.

B. Multiterminal system and transport calculation method

Our numerical calculations of the differential conductance G, LDOS $\rho(E, r_i)$, and local current distribution $J_{i\to j}$ are based on the nonequilibrium Green's function method. As sketched in Fig. 1(b), the studied wormhole system is viewed as an eight-terminal device. Each terminal is considered as a source or drain electrode. Electrons can propagate between these terminals. Here, we ignore the side surfaces during the calculation because the sample that we consider is very large and side surfaces are far from the wormholes. Generally, because the mobility of the TI material is low [32,33], injected electrons traverse long trajectories if they go through the side surfaces and thus the transmission probability is extremely low. Therefore, electronic transport is expected to happen only among the regions connected by wormholes and the current flowing through the side surface is negligible. The electric current I_n for terminal n is obtained by the Landauer-Büttiker formula [34,35]

$$I_n = (e^2/h)\sum_{m\neq n} T_{nm}(V_n - V_m), \tag{3}$$

where the transmission coefficient between terminal n and m is $T_{nm} = \mathrm{Tr}(\Gamma_n G^r \Gamma_m G^a)$ with $G^{r/a}$ the retarded/advanced Green's function of the central region. $\Gamma_{m/n} = i(\Sigma^r_{m/n} - \Sigma^a_{m/n})$ is the linewidth function at the m/n terminal with $\Sigma^{r/a}_{m/n}$ the corresponding retarded/advanced self-energy. During the calculation, we apply a small bias V between these terminals (e.g., $V_m = 0$, $V_n = V$). Then the total current I can be obtained by summing all I_n's of the source terminals. The differential conductance G is obtained by $G = dI/dV$. LDOS at site r_i can be expressed as

$$\rho(E, r_i) = -\frac{1}{\pi}\,\mathrm{Im}\,\mathrm{Tr}[G^r(E, r_i, r_i)], \tag{4}$$

where the trace is taken in the spin space and E is the energy. Local current from site i to site j is [36–38]

$$\begin{aligned} J_{i\to j} &= \frac{2e}{h}\sum_{\alpha,\beta}\sum_{n}\int_{-\infty}^{E-eV_n} dE'\,\mathrm{Im}\{H_{i\alpha,j\beta}[G^r\Gamma_n G^a]_{j\beta,i\alpha}\} \\ &\approx \frac{2e}{h}\sum_{\alpha,\beta}\int_{-\infty}^{E} dE'\,\mathrm{Im}\left\{H_{i\alpha,j\beta}\left[G^r\sum_n \Gamma_n G^a\right]_{j\beta,i\alpha}\right\} \\ &\quad -\frac{2e^2}{h}\sum_{\alpha,\beta}\mathrm{Im}\left[H_{i\alpha,j\beta}\sum_n G^n_{j\beta,i\alpha}(E)V_n\right]. \end{aligned} \tag{5}$$

V_n denotes the applied bias on terminal n and $G^n(E) = G^r(E)\Gamma_n(E)G^a(E)$. We only focus on the nonequilibrium current which corresponds to the second term in Eq. (5):

$$J^{\text{noneq}}_{i\to j} = -\frac{2e^2}{h}\sum_{\alpha,\beta}\mathrm{Im}\left[H_{i\alpha,j\beta}\sum_n G^n_{j\beta,i\alpha}(E)V_n\right]. \tag{6}$$

In order to clearly study the physical behavior of the wormholes, the influence of the finite-size effect of the top and bottom surfaces should be eliminated. The size of the surfaces should be taken as large as possible. Unfortunately, previous 3D Hamiltonians can only deal with small systems [12,16,17]. The computation advantage of our 2D model enables us to study a substantial large system (about 200 × 200 for a single-wormhole system and 300 × 300 for a double-wormhole system). Besides, we shift the Fermi energy E_F at each terminal by 0.3. In this way, the Ohmic contact between the metallic electrodes and the wormhole system becomes perfect.

III. INTERFERING TRANSPORT BETWEEN WORMHOLES

A. Double-wormhole interference

In this section, we demonstrate that the wormhole degree of freedom can be manipulated through the interfering transport in a double-wormhole system. Here, we treat terminals on the top or bottom surface as a whole. Bias V is applied between source (terminals 1–4, $V_1 = V_2 = V_3 = V_4 = V$) and drain (terminals 5–8, $V_5 = V_6 = V_7 = V_8 = 0$), as shown in Fig. 1(b). The geometry of the wormhole, for simplicity, is taken as a cuboid. The physics of the studied system is independent of the wormhole shape. In most cases, it is convenient to discretize the continuous Hamiltonian to square lattice. Therefore, considering wormholes with square shape cross sections is a natural choice.

We first calculate the band structure of an infinitely long wormhole to count how many conducting channels contribute to the differential conductance. When the magnetic flux $\phi = \pi$ (in units of $\frac{\hbar}{e}$), the wormhole is gapless and carries a pair of 1D linear modes [see insets in Fig. 2(a)]. In contrast, when ϕ is shifted from π, as shown in Fig. 2(b), a gap is opened. The linear mode of the π-flux wormhole provides a conducting channel between the top and bottom surfaces, so that in the single-wormhole system, the differential conductance $G \equiv e^2/h$. Because of the gap, G for the 0.6π-flux

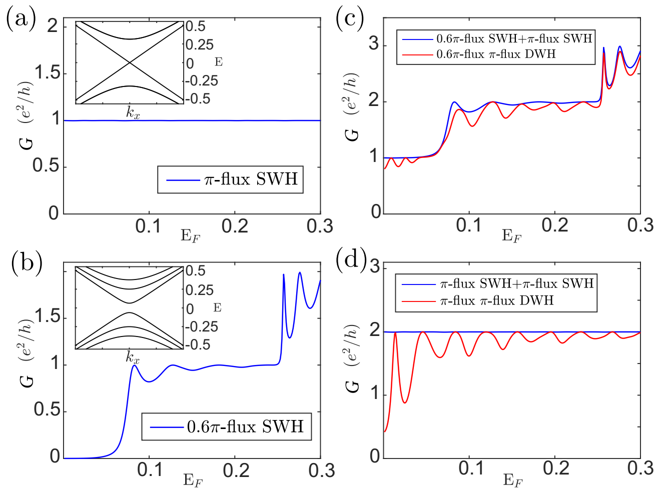

FIG. 2. (a), (b) Differential conductance G versus the Fermi energy E_F in a single-wormhole (SWH) system with magnetic flux π and 0.6π. Inset figures show the band structures of the corresponding infinitely long wormholes. (c), (d) Comparison between the single-wormhole and double-wormhole (DWH) systems in G. Distance between the two wormholes $D = 80$. In each subfigure, the blue curve is obtained by directly summing over two differential conductances of the corresponding single-wormhole systems. The red curve shows G of the double-wormhole system. The difference between the red and blue curves indicates a wormhole interference. Here, the cross-section size of the wormhole in all subfigures is 11×11, and the length $L = 100$.

single-wormhole system starts from 0 and then oscillates toward an integer conductance [Fig. 2(b)]. In a double-wormhole system, both wormholes contribute conducting channels. If the two wormholes are independent, i.e., there is no interference between them, the total differential conductance will be a naive summation $G = G_1 + G_2$ [blue curves in Figs. 2(c) and 2(d)]. $G_{1,2}$ is the differential conductance of the corresponding single-wormhole system. However, our numerical results demonstrate that G oscillates with the Fermi energy [the red curves in Figs. 2(c) and 2(d)], which implies that there is an interference between the two wormholes.

In order to see the details of the interference, we calculate the LDOS distributions $\rho(E_F, r)$ of the double-wormhole system (see Fig. 3). In the left and right panels, the LDOS distribution at the first peak and dip on the G-E_F curve are plotted. The oscillation of G is intimately related to the oscillation of ρ. For example, ρ in the wormholes is much larger at the peak than at the dip of G. The rising of ρ also indicates that there is resonant tunneling between the top and bottom surfaces modulated by the wormhole interference.

We further investigate the geometrical dependence of double-wormhole interference. In the following, we compare the differential conductance G by varying the distance D, length L, and the cross-section size of the wormholes.

As shown in Fig. 4(a), G with different cross-section sizes almost coincide with each other when $E_F < 0.2$. Therefore, the cross-section sizes of wormholes have almost no influence on the double-wormhole interference. Nevertheless, the cross-section size still plays a role in tuning the wormhole degree of freedom. The green curve jumps when $E_F > 0.2$ because a wider wormhole provides more confined subbands (for a cylindrical TI nanowire with radius R, the energy difference between confined subband $\propto 1/R$ [17]). The Fermi energy E_F crosses three subbands (including two degenerate subbands) for each wormhole. There are six conducting channels, and G reaches $6e^2/h$.

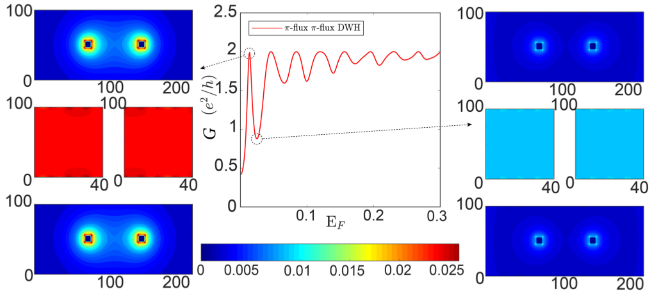

FIG. 3. LDOS distribution $\rho(E_F, r)$ of the double-wormhole system with two π-flux wormholes. The G-E_F curve takes from Fig. 2(d). The LDOS distribution $\rho(E_F, r)$ at the first peak and dip on the G-E_F curve are plotted correspondingly. In each subplot, the top and bottom panels correspond to the top and bottom surfaces. The two small panels in the middle represent the expanded side surfaces of the two wormholes.

Figures 4(b) and 4(c) show the behavior of the wormhole interference with fixed cross-section size (11×11) by varying D and L. As plotted in Fig. 4(b), the interference becomes stronger when the two wormholes get closer, so that the amplitude of the oscillation in G is enhanced. Meanwhile,

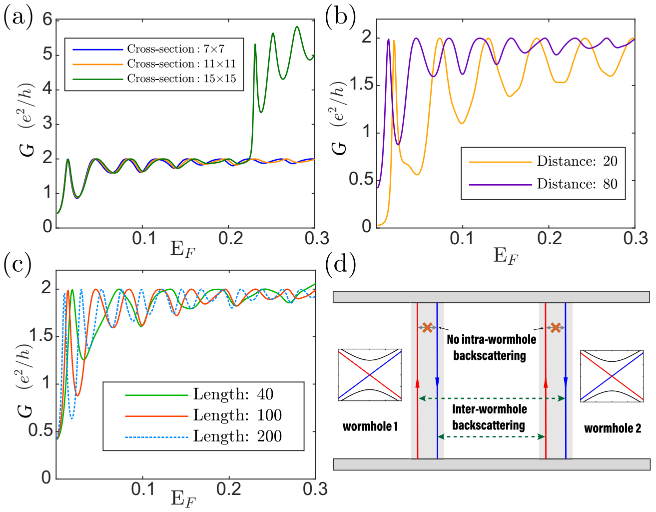

FIG. 4. Geometrical dependence of the double-wormhole interference. (a) The differential conductance G of double-wormhole systems with different cross-section size. The length of the wormhole $L = 100$ and the distance between them $D = 80$. (b) G versus E_F under different D with $L = 100$. (c) G versus E_F by varying L, with fixed $D = 80$. The cross-section size in (b) and (c) takes 11×11. (d) Schematic of the interwormhole backscattering process between two π-flux wormholes. Red (blue) arrowed lines inside the wormholes represent upward (downward) linear modes. Backscattering of linear modes can (cannot) happen between interwormholes (intrawormholes).

enlarging L and D can visibly suppress the oscillation period [see Figs. 4(b) and 4(c)]. The L and D dependence of the oscillation can be phenomenologically explained by considering the double-wormhole system as an effective Aharonov-Bohm ring [39,40], where the two wormholes together with the top and bottom surfaces form a closed path, and the total perimeter is $2(L + D)$. The resonance tunneling happens when $2k_F(L + D) = 2\pi(n + 1/2)$, where k_F is the wave vector at E_F, n is an integer, and $\frac{1}{2}$ originates from the geometrical phase of the linear band. The oscillation period ΔE equals to the energy difference between neighbor resonance peaks, thus, $\Delta E = \hbar v_F \Delta k_F = 2\pi\hbar v_F/2(L + D)$. Therefore, the oscillation of G is faster for the double-wormhole system with longer wormhole length L or distance D.

In order to better understand the interference phenomenon in double-wormhole systems and the formation of the effective AB ring, we propose an interwormhole backscattering mechanism, as sketched in Fig. 4(d). The π-flux wormhole carries a pair of gapless linear modes that are protected by the topological bulk and the induced magnetic flux ϕ. Due to the Klein tunneling [41], there is no backscattering between the two linear modes in a π-flux wormhole, and $G \equiv e^2/h$ is observed [Fig. 2(c)]. When $\phi \neq \pi$, the two modes are coupled, and a gap is opened in the energy spectrum [see inset in Fig. 2(b)]. This coupling induces a backscattering between the two linear modes (intrawormhole backscattering) and causes the oscillation of G even in a single-wormhole system [see G-E_F curve in Fig. 2(b)]. In a double-wormhole system with two π-flux wormholes, there is no intrawormhole backscattering. However, linear modes of different wormholes are coupled with each other through the top and bottom surfaces. This coupling results in an interwormhole backscattering [see dashed arrows in Fig. 4(d)] and can also lead to the oscillation of G. The closer the wormholes are, the stronger the coupling between the backscattering channels is, thus the oscillation amplitude of G is enhanced [Fig. 4(b)]. Furthermore, because of the interwormhole backscattering, electrons can travel between wormholes and their spatial trajectory form a closed loop [see Fig. 4(d)], thus the double-wormhole system can be viewed as an effective AB ring.[3]

B. Multiwormhole interference

In this section, we show that unique transport phenomena can be obtained through changing the number of wormholes. Particularly, we find that the differential conductance G shows a parity dependence on the number of wormholes. It originates from the fact that the physics behind the interwormhole backscattering is the same as the backscattering between the helical edge modes in 2D TIs, and falls into a $\mathbb{Z}_2$ classification [42].

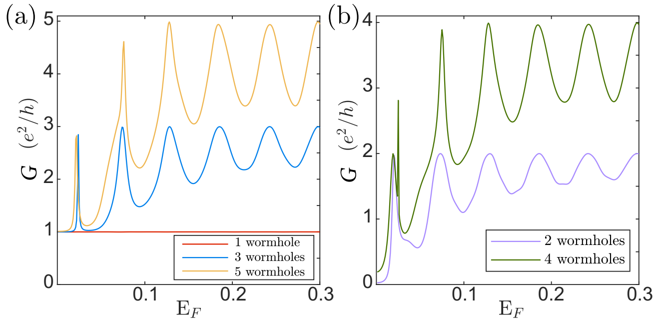

FIG. 5. G-E_F for multiwormhole systems. Wormholes are lined up with distance $D = 20$, and wormhole length $L = 100$. (a) Multiwormhole systems with 1, 3, 5 wormholes. $G \geqslant e^2/h$, indicating at least one conducting channel survives. (b) Multiwormhole systems with 2, 4 wormholes. G can be smaller than e^2/h.

On the edge of 2D TIs, the forward edge mode cannot be backscattered into its time-reversal counterpart (the corresponding helical counterpart), but can be backscattered into backward edge modes that belong to different Kramers pairs. This backscattering mechanism leads to a $\mathbb{Z}_2$ classification for time-reversal-invariant materials [43]. A system with an even (odd) number of helical edge mode Kramers pairs is categorized into a $\mathbb{Z}_2 = 0$ ($\mathbb{Z}_2 = 1$) class, which is equivalent to a normal (topological) insulator. In normal insulators, the backscattering can destroy all conducting channels, and the minimum of G falls to 0. On the contrary, in TIs there is always one protected gapless edge mode survives the backscattering, thus, $G \geqslant e^2/h$.

Interestingly, the multiwormhole system (all wormholes are π flux) reproduces this $\mathbb{Z}_2$ classification through the wormhole backscattering. A pair of linear modes in each wormhole can be considered as a Kramers pair of helical edge modes, and the intrawormhole (interwormhole) backscattering is forbidden (allowed). In analogy with the 2D TI, multiwormhole systems with odd (even) number of wormholes are expected to be in the $\mathbb{Z}_2 = 1$ ($\mathbb{Z}_2 = 0$) or "topological" ("normal") classification. Our numerical simulations of multiwormhole systems with 1, 3, 5 and 2, 4 wormholes strongly confirm these expectations [see Figs. 5(a) and 5(b)]. For multiwormhole systems with an odd number of wormholes, $G \geqslant e^2/h$ is observed [Fig. 5(a)]. It is consistent with the "topological" case ($\mathbb{Z}_2 = 1$) where one protected mode survives the interwormhole backscattering. By contrast, as shown in Fig. 5(b), G-E_F curves of systems with an even number of wormholes start from $G \approx 0$. It belongs to the "normal" case ($\mathbb{Z}_2 = 0$), where no conducting mode survives the interwormhole backscattering.

The modulation of G through changing the number of wormholes provides a different way to manipulate the wormhole degree of freedom, enabling wormhole systems to be more controllable in topological device applications. Moreover, as far as we know, because of difficulties in transport experiments, the $\mathbb{Z}_2$ characteristics have not yet been observed in the quantum spin Hall systems experimentally. We believe that the multiwormhole provides a clean platform to investigate the relevant $\mathbb{Z}_2$ physics by changing the wormhole numbers.

---

[3] The multiple TI nanowire system is of no reason to be similar to our multiwormhole system. From the transport point of view, because of the dephasing effect of the external leads, multiple TI nanowires contribute to the total conductance incoherently. Our numerical results show a synergy of wormholes and topological surfaces that brings interference effect between wormholes.

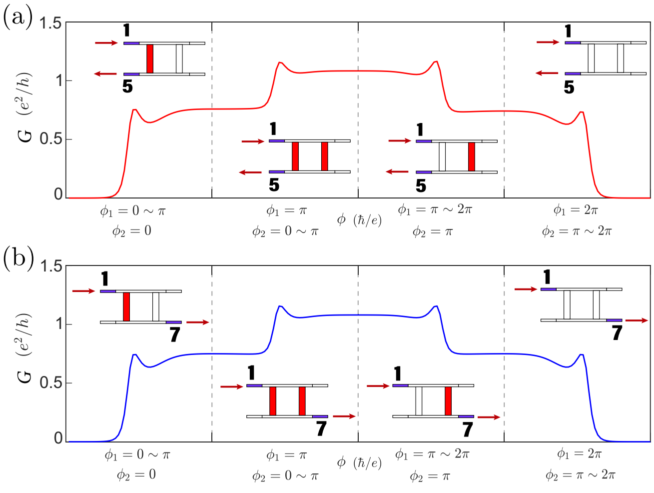

FIG. 6. G of "wormhole switch" device by alternately varying ϕ in the two wormholes. Here, $E_F = 0.1$, $D = 80$, $L = 100$ and the cross-section size takes 11×11. In each inset, the red (white) colored area represents a conducting (insulating) wormhole. Terminal 1 (5) in (a) and terminal 1 (7) in (b) are taken as source (drain) with all the other terminals set float.

IV. TOPOLOGICAL DEVICES BASED ON THE WORMHOLE EFFECT

In this section, we show that the manipulation of the wormhole degree of freedom makes the wormhole systems feasible in designing topological devices. Specifically, we propose two types of devices: (1) the "wormhole switch," which controls the transport behavior of the device by varying the magnetic flux ϕ; (2) the "traversable wormhole" device, which provides conducting channels and enables electrons to travel across the surface separated by obstacles.

A. "Wormhole switch" device

By manipulating the wormhole degree of freedom through varying ϕ, the conducting and insulating status of wormholes can be switched. This phenomenon inspires us to utilize wormhole systems as switches in topological devices. In this section, we study such an application by investigating the ϕ dependence of double-wormhole systems.

Here we pick two of the eight terminals as external leads and set all the other terminals open. Two cases are considered, where the electric current comes from lead 1 and leaves at lead 5 or lead 7 (see insets of Fig. 6). Figures 6(a) and 6(b) plot the differential conductance G versus ϕ in the two wormholes. For both cases, $G = 0$ in the absence of ϕ, signaling the insulating status between the top and bottom surfaces. By alternately varying ϕ of the two wormholes, G jumps steeply and then manifests a plateaulike behavior. This phenomenon means that the system can be steadily switched between the conducting (on) and insulating (off) status. In fact, we can not only switch the on and off status of the topological device, but also switch the spatial distribution of the current on each wormhole. By calculating the local current distribution (here, terminals 1 and 5 are chosen as the source and drain), we find a "remote tunneling" phenomenon, as shown in Fig. 7(a). The near wormhole is "turned off" and the distant wormhole is "turned on." The electric current coming from terminal 1 bypassing the near wormhole then flows through the distant conducting wormhole to terminal 5. For comparison, Fig. 7(b) shows the case where both wormholes are turned on. More electric current flows through the near wormhole (about 55%) than through the distant wormhole (about 45%). In applications, the controllable of the current distribution enables us to integrate complex topological devices, which can realize various transport functions among different places.

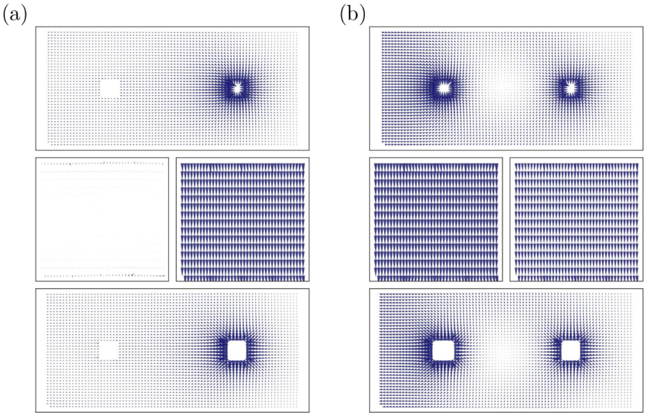

FIG. 7. Local current distribution of the "wormhole switch" device. In both subfigures, the upper and lower panels correspond to the top and bottom surfaces. The middle two panels correspond to the expanded side surfaces of the wormholes. Terminals 1 and 5 are chosen as the source and drain. Device size and E_F are the same as Fig. 6(a). (a) $\phi_1 = 0$ and $\phi_2 = \pi$. (b) $\phi_1 = \phi_2 = \pi$.

More figuratively, the wormhole provides a "bridge" that connects opposite surfaces of the TI and makes electrons traveling between them possible. Thus, the wormhole in TIs resembles the real wormhole in general relativity. The difference is that in TIs, the wormhole degree of freedom is highly tunable by varying the magnetic fluxes. In applications, we can switch not only the on and off status, but also the current distribution of the topological device.

B. "Traversable wormhole" device

Apart from connecting the opposite surfaces isolated by the insulating bulk, the wormhole in TIs can also provide conducting channels to connect the separated regions of the same surface. In real topological devices, the transport of electrons on the same surface of TI is not always unimpeded. For example, the metallic surface state may be destroyed by magnetic impurities, or separated by lumps, external leads, and other complicated device structures [e.g., see Fig. 8(a)]. Thus, electrons cannot pass through these obstacles. In order to make the electronic transport between the separated regions possible, similar as the space traveling between separated space-time [44], we propose a "traversable wormhole" device. The obstacles on the surface of TI are modeled by a cutting off in the middle on the top surface so that electrons cannot transport across it directly [see Fig. 8(b)]. The local current distribution [see Fig. 8(e)] shows clearly that electric current comes from the source (terminal 1) flows to the bottom surface

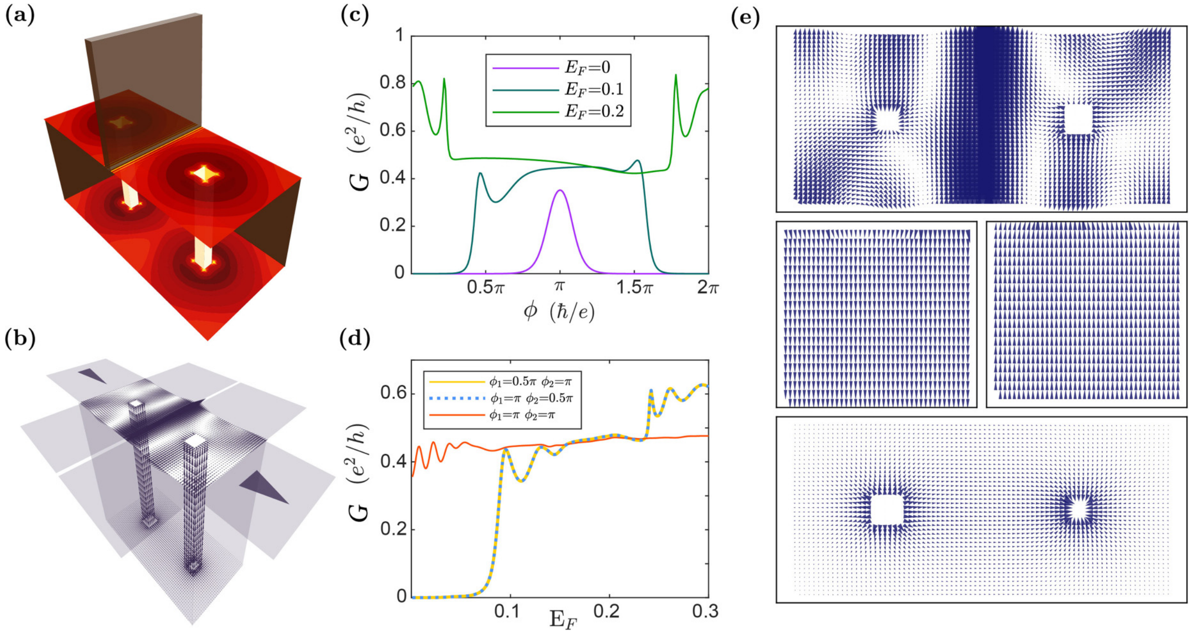

FIG. 8. (a) Sketch of a "traversable wormhole" device. (b) Schematic of the current distribution in the traversable wormhole device. Electric current flows from terminal 1 traveling across the two conducting wormholes, then to terminal 3. The separated regions in the top surface of TI are connected by wormholes. (c) G as a function of the magnetic flux ϕ at different E_F. $\phi_1 = \phi_2 = \phi$. (d) G as a function of E_F. Three different combinations of ϕ_1 and ϕ_2 are compared. (e) Local current distribution of the traversable wormhole device with $\phi_1 = \phi_2 = \pi$ and $E_F = 0.1$. The top surface is separated in the middle, the conducting wormhole pair serves as a bridge that connects the separated top surface. Device size is the same as Fig. 6.

through the near wormhole, then flows back to the drain on the top surface (terminal 3) through the distant wormhole, completes a "wormhole traveling."

Furthermore, we investigate the transport performance of the device in detail. As shown in Fig. 8(c), the differential conductance G can be modulated by simultaneously varying the magnetic fluxes of both wormholes with a fixed E_F. We find that the conducting region falls into a flux window centered at π. The jump of G from 0 to a finite value means that the separate regions are connected by wormholes. The width of the flux window is enlarged with the increasing of E_F, signaling the tunability of the "traversable wormhole" device. Then we compare G under three combinations of the magnetic fluxes ϕ_1 and ϕ_2 [Fig. 8(d)]. The wormhole traveling phenomenon happens at any E_F only if both wormholes are π flux. This is because only when E_F crosses the subbands of both wormholes [see insets Figs. 2(a) and 2(b)] can the two wormholes provide a conducting channel for the electron to complete a wormhole traveling process.

In applications, the "traversable wormhole" device can bridge TI surfaces that are separated by obstacles. For example, when a TI thin film is fabricated on the substrate, the bottom surface of the thin film is sealed and maintains excellent transport performance. However, its top surface is exposed to the environment or is used to build complex device structures. Thus, the electron transport on the top surface may be impeded. Fortunately, with the help of the traversable wormhole device, electrons can still travel across the top surface. Moreover, through varying E_F or ϕ of the wormholes, the traveling can be finely controlled.

V. CONCLUSION AND PERSPECTIVE

In summary, we have numerically studied the wormhole system by applying the 2DELH. We find that the "wormhole effect," as a unique degree of freedom, can manipulate the transport properties of TIs. The oscillation of the differential conductance G and the LDOS in the double-wormhole system demonstrated an interfering transport between the wormholes, depending on the system geometry. The interference phenomenon originates from the interwormhole backscattering. Electrons can be backscattered between the wormholes to complete the motion in a closed path, causing an effective AB interference. Furthermore, by studying the multiwormhole systems, we find that the interwormhole backscattering mechanism leads to a $\mathbb{Z}_2$ classification, and G shows a parity dependence on the number of wormholes. Therefore, the transport properties of the system can be modulated by the wormhole numbers.

We then propose two topological device applications through the manipulation of the wormhole degree of freedom. The first one is the "wormhole switch" device, which enables us to switch not only the on and off status, but also the current distribution of the device through varying the magnetic fluxes of the wormholes. The second one is the "traversable wormhole" device, which provides conducting channels to connect isolated regions of the topological surfaces. It enables electrons to complete a "wormhole traveling" and bypass the obstacles on the surface.

Recently, transport experiments based on semiconductor, 2D TI quantum well, or superconductor thin films with

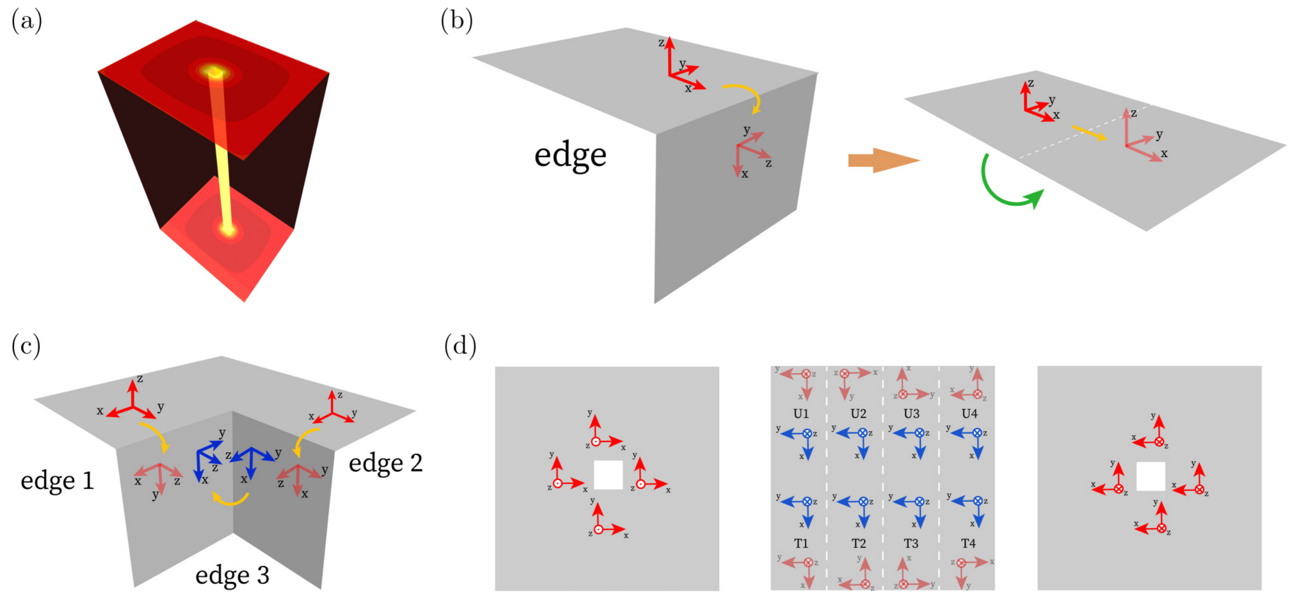

FIG. 9. (a) Sketch of a single-wormhole system. (b) A bent surface with one edge can be flattened. The local coordinate frame is parallelly translated along the surface. (c) A cornerlike surface can be viewed as three sets of bent surfaces. The red (blue) colored coordinate frame represents the local coordinate frame on the top (side) surface. The light red colored ones represent the coordinate frames parallelly translated from the top surface. (d) Coordinate frame specified on the top surface (left panel), the surface of the wormhole (middle panel), and bottom surface (right panel). The z direction is the outward normal direction on each surface (here the outward means the axis points from the bulk to the vacuum). Red (blue) colored frames represent local coordinate frames on the top and bottom surfaces (on the wormhole). Light red colored frames are obtained by parallelly translating frames from top and bottom surfaces to the wormhole. The four slices of the wormhole surface are connected to the top surface in order of left-down-right-up. U_i and T_i indicate the unitary transformations of the corresponding spinor basis on the edges.

nanopore structures have been reported [45–47]. We expect that the TI thin film with nanopore structures can serve as an ideal platform to realize the wormhole devices. Since the radius of the etched nanopores is reported to be around 50–100 nm, the applied magnetic field required for a flux quantum is expected to be less than 0.25 T.[4] Therefore, the wormhole devices and the manipulations of the wormhole degree of freedom are highly achievable in experiments. Other potential candidates to realize the wormhole systems are the artificial structures such as the photonic and phononic crystals [48–52] and the topological electric circuit [53,54], which have attracted extensive attention. Especially, the 3D photonic topological insulator [55] and the 3D acoustic TI [56] have been realized recently. The macroscopic scale of these structures makes it easier to build the tubular geometry of the wormholes. Moreover, introducing and controlling the magnetic fluxes are feasible in classical wave systems [53,54,57–60]. For these reasons, artificial structures provide flexible platforms for physicists to investigate the novel properties of the wormhole systems.

ACKNOWLEDGMENTS

We thank Y.-F. Zhou and H.-M. Guo for fruitful discussion. This work is financially supported by the National Basic Research Program of China (Grants No. 2017YFA0303301 and No. 2019YFA0308403) and the National Natural Science Foundation of China (Grants No. 11534001, No. 11674028, No. 11822407, No. 11921005, and No. 12022407).

APPENDIX A: CONSTRUCTION OF LATTICE HAMILTONIAN FOR THE WORMHOLE SYSTEM

As have been discussed in Refs. [27,28], the Dirac Hamiltonian $H(\mathbf{r})$ on a 2D curved surface is not trivial since H inherits geometrical and topological information of the surface. It brings difficulties in numerical calculations when H is discretized into a lattice form. In this Appendix, we propose a simple method to deal with the discretized $H(\mathbf{r})$ on a curved surface by dividing the whole surface into a set of flat surfaces and glue them together by unitary transformations on spinor basis at the edges. Then, we give the exact form of the transformation matrices. This method can also be generalized to higher dimensions.

In order to encode geometric information into the Hamiltonian $H(\mathbf{r})$, partial derivatives ∂_k in the momentum term should be replaced by covariant derivatives [27], which generates the parallel translations of the spinor basis on the

---

[4] We note that the applied magnetic field is not necessarily restricted to the wormhole only. Because only surface states are involved, the total magnetic flux in the wormhole is determined by the field strength and the cross-section area of the wormhole rather than the area over which the magnetic field is applied. Nevertheless, the area over which the magnetic field is applied cannot be too large to avoid the formation of Landau levels on the top and bottom surfaces. Given that, the magnetic field can be applied over an area suitably larger than the wormhole.

curved surface. As shown in Fig. 9(b), a bent surface can be flattened because of its zero curvature ($\Omega = 0$). The local coordinate frame on the flat surface can be parallelly translated without the additional information of Ω. This is why the surface of an infinite long TI tube can be flattened [19,61], except for an antiperiodic boundary condition that we will discuss soon.

In contrast, for curved surfaces with nonzero Ω such as the cornerlike surface plotted in Fig. 9(c) (the cross point of the three edges is a singular point of Ω), the flattening procedure can no longer be performed. Consequently, the parallel translations of local spinor basis cannot be unified on the three edges (they "frustrate" each other), and at least two of the frames should be related by a nontrivial coordinate transformation [coordinate frames on the 1-3 surface (determined by edge 1 and edge 3) in Fig. 9(c)]. In the wormhole system, cornerlike structures appear when the wormhole crosses the top and bottom surfaces. The planar graph of a single-wormhole system with specified local coordinate frames is shown in Fig. 9(d) (colored red for the top and bottom surfaces and blue for the wormhole). The light red colored coordinate frames are parallelly translated from top and bottom surfaces to the wormhole. Obviously, these frames are not always coincident with the blue colored frames, and coordinate transformations are inevitable.

When $H(\mathbf{r})$ is discretized into a lattice form, the parallel translation operations are reflected in the hopping terms. To be clear, we consider an electron hopping process from the top surface of the cornerlike structure in Fig. 9(c), to the 1-3 side surface. The wave function components after hopping are obtained by projecting the electron state onto the blue colored spinor basis on the wormhole, instead of the parallelly translated spinor basis (light red colored). Thus, wave functions before and after hopping should be related by a unitary transformation.

For the wormhole system, as shown in Fig. 9(d), parallel translation of spinor basis between different coordinate frame induces a set of unitary transformations between the wormhole and the top (bottom) surface denoted by U_i (T_i), respectively, where $i = 1, 2, 3, 4$. They can be obtained as follows. Suppose the local spinor basis on the top surface is $|\mathbf{e}^t_\mu\rangle$ ($\mu = \uparrow, \downarrow$ represents the $+z$ or $-z$ direction, similarly hereinafter), the four side surfaces of the wormhole are denoted by a,b,c,d on which the local spinor basis are $|\mathbf{a}^w_\mu\rangle$, $|\mathbf{b}^w_\mu\rangle$, $|\mathbf{c}^w_\mu\rangle$, and $|\mathbf{d}^w_\mu\rangle$. The parallelly translated spinor bases from the top surface to the side surfaces of the wormhole a denoted by $|\mathbf{a}^t_\mu\rangle$, $|\mathbf{b}^t_\mu\rangle$, $|\mathbf{c}^t_\mu\rangle$, and $|\mathbf{d}^t_\mu\rangle$. For example, when an electron state $|\psi\rangle = \sum_\mu |\mathbf{e}^t_\mu\rangle v^\mu$ on the top surface is parallelly translated to the side surface b, the translated state is $|\psi^t\rangle = \sum_\mu |\mathbf{b}^t_\mu\rangle v^\mu$. Notice that in numerical calculations, the wave functions after hopping is expressed under the $|\mathbf{b}^w_\mu\rangle$ basis, thus the unitary transformation from $|\mathbf{b}^t_\mu\rangle$ to $|\mathbf{b}^w_\mu\rangle$ is needed. They can be obtained by noticing that $|\psi^t\rangle = \sum_\mu |\mathbf{b}^t_\mu\rangle v^\mu = \sum_\mu \sum_\nu |\mathbf{b}^w_\nu\rangle\langle \mathbf{b}^w_\nu|\mathbf{b}^t_\mu\rangle v^\mu = \sum_\mu \sum_\nu |\mathbf{b}^w_\nu\rangle U_{\nu\mu} v^\mu$ and the transformation matrix is $U_{\nu\mu} = \langle \mathbf{b}^w_\nu|\mathbf{b}^t_\mu\rangle$. Importantly, the parallelly translated basis $|\mathbf{b}^t_\mu\rangle$ can be obtained by rotating the original basis $|\mathbf{e}^t_\mu\rangle$ and we have $|\mathbf{b}^t_\mu\rangle = \hat{\mathbf{R}}_{b\leftarrow e}|\mathbf{e}^t_\mu\rangle$, $\hat{\mathbf{R}}_{b\leftarrow e}$ is a rotation operator. Here, we define that the local bases are related by $|\mathbf{a}^w_\mu\rangle = |\mathbf{a}^t_\mu\rangle = \hat{\mathbf{R}}_{a\leftarrow e}|\mathbf{e}^t_\mu\rangle$ and $|\mathbf{b}^w_\mu\rangle = \hat{\mathbf{R}}_{b\leftarrow a}|\mathbf{a}^w_\mu\rangle$, $|\mathbf{c}^w_\mu\rangle = \hat{\mathbf{R}}_{c\leftarrow b}|\mathbf{b}^w_\mu\rangle$, $|\mathbf{d}^w_\mu\rangle = \hat{\mathbf{R}}_{d\leftarrow c}|\mathbf{c}^w_\mu\rangle$. From these relations we can write the matrix form of U as

$$\begin{aligned} U_{\mu\nu} &= \langle \mathbf{b}^w_\mu|\mathbf{b}^t_\nu\rangle \\ &= \langle \mathbf{b}^w_\mu|\hat{\mathbf{R}}_{b\leftarrow e}\hat{\mathbf{R}}^\dagger_{a\leftarrow e}\hat{\mathbf{R}}^\dagger_{b\leftarrow a}|\mathbf{b}^w_\nu\rangle. \end{aligned} \tag{A1}$$

From Eq. (A1) we can calculate the exact form of the unitary transformation between the top surface and the side surface b on the wormhole. Express $\hat{\mathbf{R}}$ under the $|\mathbf{b}^w_\mu\rangle$ basis (for example, the matrix form of $\hat{\mathbf{R}}_{b\leftarrow e}$ rotation is $e^{-i\frac{\sigma_y}{4}\pi}$), we have

$$U_2 = U_y\left(\frac{\pi}{2}\right)U_z\left(-\frac{\pi}{2}\right)U_x\left(\frac{\pi}{2}\right) = U_z\left(-\frac{\pi}{2}\right), \tag{A2}$$

where $U_{x,y,z}(\phi) = e^{-i\frac{\sigma_{x,y,z}}{2}\phi}$. After similar analysis, we can also obtain the unitary transformations between the top surface and the a,c,d side surfaces on the wormhole, with

$$\begin{aligned} U_1 &= I_{2\times 2}, \\ U_3 &= U_y\left(\frac{\pi}{2}\right)U_y\left(\frac{\pi}{2}\right)U_x(\pi) = U_z(-\pi), \\ U_4 &= U_y\left(\frac{\pi}{2}\right)U_z\left(\frac{\pi}{2}\right)U_x\left(\frac{3\pi}{2}\right) = U_z\left(-\frac{3\pi}{2}\right). \end{aligned} \tag{A3}$$

Then, the unitary transformations between the bottom surface and the wormhole are

$$\begin{aligned} T_1 &= I_{2\times 2}, \\ T_2 &= U_x\left(\frac{\pi}{2}\right)U_z\left(-\frac{\pi}{2}\right)U_y\left(-\frac{\pi}{2}\right) = U_z\left(-\frac{\pi}{2}\right), \\ T_3 &= U_y\left(-\frac{\pi}{2}\right)U_z(-\pi)U_y\left(-\frac{\pi}{2}\right) = U_z(-\pi), \\ T_4 &= U_x\left(-\frac{\pi}{2}\right)U_z\left(-\frac{3\pi}{2}\right)U_y\left(-\frac{\pi}{2}\right) = U_z\left(-\frac{3\pi}{2}\right). \end{aligned} \tag{A4}$$

For the last step, the flat surface should be rolled up into a tube and forms the wormhole. The antiperiodic boundary condition should be applied [19] because after a 2π rotation, the spinor basis changes by a π-phase factor. Therefore, the unitary transformation, in this case, is just $-\mathbf{I}$. Physically it can also be understood as a π geometrical phase induced by the rotation of spinors [62].

APPENDIX B: PROPERTIES OF SINGLE-WORMHOLE SYSTEMS

In this Appendix, we investigate the properties of a single-wormhole system and check the validity of the 2DELH. The corresponding LDOS of a π-flux wormhole system is studied [Fig. 10(a)]. Figures 10(d) and 10(e) plot the energy dispersions of the infinite long wormhole and the infinite large surface. Figures 10(b) and 10(c) show the LDOS at fixed points on the top surface and on the wormhole. As expected, the total density of states ρ is a linear function of E for the topological surface due to 2D Dirac cone dispersion, and a constant for the π-flux wormhole due to 1D linear dispersion. Our numerical results perfectly match this expectation, therefore, establish our confidence for further calculations based on this 2DELH.

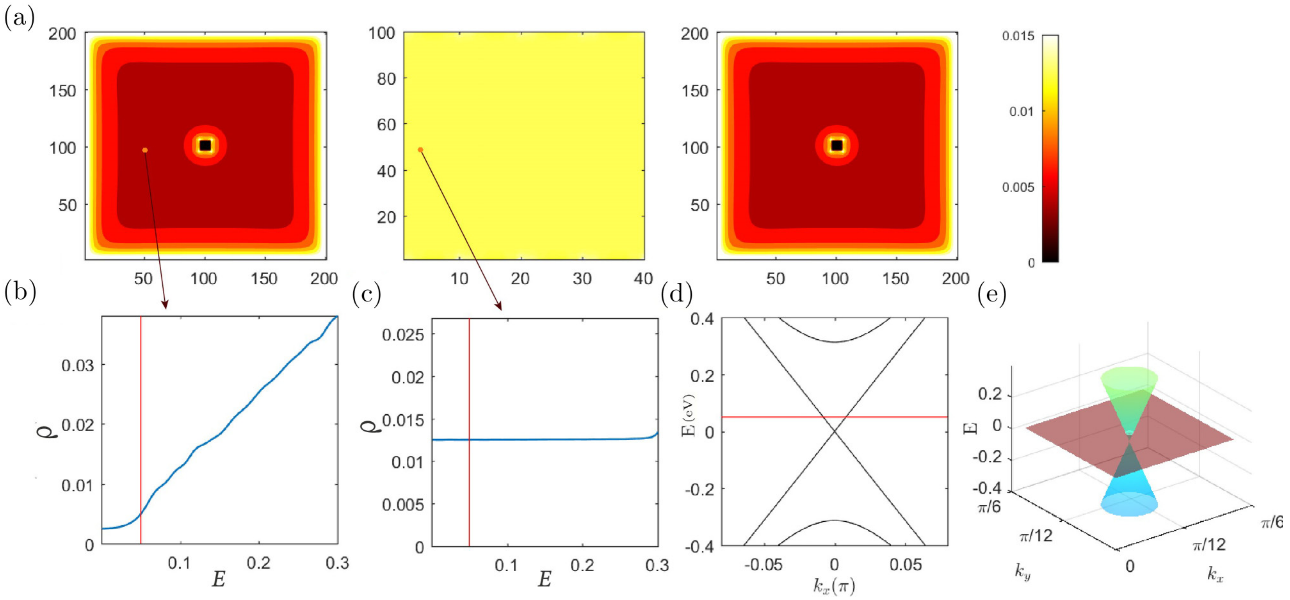

FIG. 10. (a) LDOS ρ of the single-wormhole system at Fermi energy $E_F = 0.05$. (b) ρ-E at a fixed point on the surface. (c) ρ-E at a fixed point on the wormhole. (e) Energy dispersion of an infinitely long wormhole. (f) Energy dispersion of a TI surface. The cross-section size of the wormhole takes 11×11, the wormhole length $L = 100$. The red lines (surface) in (b)–(e) represent the Fermi energy.

[1] M. Z. Hasan and C. L. Kane, *Colloquium:* Topological insulators, Rev. Mod. Phys. **82**, 3045 (2010).

[2] X.-L. Qi and S.-C. Zhang, Topological insulators and superconductors, Rev. Mod. Phys. **83**, 1057 (2011).

[3] L. Fu, C. L. Kane, and E. J. Mele, Topological Insulators in Three Dimensions, Phys. Rev. Lett. **98**, 106803 (2007).

[4] L. Fu and C. L. Kane, Topological insulators with inversion symmetry, Phys. Rev. B **76**, 045302 (2007).

[5] J. E. Moore and L. Balents, Topological invariants of time-reversal-invariant band structures, Phys. Rev. B **75**, 121306(R) (2007).

[6] Y. L. Chen, J. G. Analytis, J.-H. Chu, Z. K. Liu, S.-K. Mo, X. L. Qi, H. J. Zhang, D. H. Lu, X. Dai, Z. Fang *et al.*, Experimental realization of a three-dimensional topological insulator, Bi_2Te_3, Science **325**, 178 (2009).

[7] H. Zhang, C.-X. Liu, X.-L. Qi, X. Dai, Z. Fang, and S.-C. Zhang, Topological insulators in Bi_2Se_3, Bi_2Te_3 and Sb_2Te_3 with a single Dirac cone on the surface, Nat. Phys. **5**, 438 (2009).

[8] Y. Xia, D. Qian, D. Hsieh, L. Wray, A. Pal, H. Lin, A. Bansil, D. Grauer, Y. S. Hor, R. J. Cava *et al.*, Observation of a large-gap topological-insulator class with a single Dirac cone on the surface, Nat. Phys. **5**, 398 (2009).

[9] Y. Zhang and A. Vishwanath, Anomalous Aharonov-Bohm Conductance Oscillations from Topological Insulator Surface States, Phys. Rev. Lett. **105**, 206601 (2010).

[10] R. Egger, A. Zazunov, and A. L. Yeyati, Helical Luttinger Liquid in Topological Insulator Nanowires, Phys. Rev. Lett. **105**, 136403 (2010).

[11] S. S. Hong, Y. Zhang, J. J. Cha, X.-L. Qi, and Y. Cui, One-dimensional helical transport in topological insulator nanowire interferometers, Nano Lett. **14**, 2815 (2014).

[12] S. Cho, B. Dellabetta, R. Zhong, J. Schneeloch, T. Liu, G. Gu, M. J. Gilbert, and N. Mason, Aharonov–Bohm oscillations in a quasi-ballistic three-dimensional topological insulator nanowire, Nat. Commun. **6**, 7634 (2015).

[13] L.-X. Wang, C.-Z. Li, D.-P. Yu, and Z.-M. Liao, Aharonov–Bohm oscillations in Dirac semimetal Cd_3As_2 nanowires, Nat. Commun. **7**, 10769 (2016).

[14] B.-C. Lin, S. Wang, L.-X. Wang, C.-Z. Li, J.-G. Li, D. Yu, and Z.-M. Liao, Gate-tuned Aharonov-Bohm interference of surface states in a quasiballistic Dirac semimetal nanowire, Phys. Rev. B **95**, 235436 (2017).

[15] J. Ying, G. Yang, Z. Lyu, G. Liu, Z. Ji, J. Fan, C. Yang, X. Jing, H. Yang, L. Lu, and F. Qu, Gate-tunable h/e-period magnetoresistance oscillations in Bi_2O_2Se nanowires, Phys. Rev. B **100**, 235307 (2019).

[16] K.-I. Imura and Y. Takane, Protection of the surface states in topological insulators: Berry phase perspective, Phys. Rev. B **87**, 205409 (2013).

[17] G. Rosenberg, H.-M. Guo, and M. Franz, Wormhole effect in a strong topological insulator, Phys. Rev. B **82**, 041104(R) (2010).

[18] L. V. Keldysh, Diagram technique for nonequilibrium processes, Sov. Phys.–JETP **20**, 1018 (1965) [ZhETF **47**, 1515 (1965)].

[19] Y.-F. Zhou, H. Jiang, X. C. Xie, and Q.-F. Sun, Two-dimensional lattice model for the surface states of topological insulators, Phys. Rev. B **95**, 245137 (2017).

[20] H. B. Nielsen and M. Ninomiya, Absence of neutrinos on a lattice: (i). proof by homotopy theory, Nucl. Phys. B **185**, 20 (1981).

[21] H. B. Nielsen and M. Ninomiya, A no-go theorem for regularizing chiral fermions, Phys. Lett. B **105**, 219 (1981).

[22] J. B. Kogut, The lattice gauge theory approach to quantum chromodynamics, Rev. Mod. Phys. **55**, 775 (1983).

[23] D. J. J. Marchand and M. Franz, Lattice model for the surface states of a topological insulator with applications to magnetic and exciton instabilities, Phys. Rev. B **86**, 155146 (2012).

[24] J. Tworzydlo, C. W. Groth, and C. W. J. Beenakker, Finite difference method for transport properties of massless Dirac fermions, Phys. Rev. B **78**, 235438 (2008).

[25] H.-Z. Lu, J. Shi, and S.-Q. Shen, Competition Between Weak Localization and Antilocalization in Topological Surface States, Phys. Rev. Lett. **107**, 076801 (2011).

[26] E. I. Blount, Bloch electrons in a magnetic field, Phys. Rev. **126**, 1636 (1962).

[27] D.-H. Lee, Surface States of Topological Insulators: The Dirac Fermion in Curved Two-Dimensional Spaces, Phys. Rev. Lett. **103**, 196804 (2009).

[28] Y. Takane and K.-I. Imura, Unified description of dirac electrons on a curved surface of topological insulators, J. Phys. Soc. Jpn. **82**, 074712 (2013).

[29] R. Kozlovsky, A. Graf, D. Kochan, K. Richter, and C. Gorini, Magnetoconductance, Quantum Hall Effect, and Coulomb Blockade in Topological Insulator Nanocones, Phys. Rev. Lett. **124**, 126804 (2020).

[30] O. Vafek, Quantum Hall effect in a singly and doubly connected three-dimensional topological insulator, Phys. Rev. B **84**, 245417 (2011).

[31] K.-I. Imura, Y. Yoshimura, Y. Takane, and T. Fukui, Spherical topological insulator, Phys. Rev. B **86**, 235119 (2012).

[32] G. Kunakova, L. Galletti, S. Charpentier, J. Andzane, D. Erts, F. Leonard, C. D. Spataru, T. Bauch, and F. Lombardi, Bulk-free topological insulator $\mathrm{Bi_2Se_3}$ nanoribbons with magnetotransport signatures of dirac surface states, Nanoscale **10**, 19595 (2018).

[33] K.-B. Han, S. K. Chong, A. O. Oliynyk, A. Nagaoka, S. Petryk, M. A. Scarpulla, V. V. Deshpande, and T. D. Sparks, Enhancement in surface mobility and quantum transport of $\mathrm{Bi_{2-x}Sb_xTe_{3-y}Se_y}$ topological insulator by controlling the crystal growth conditions, Sci. Rep. **8**, 17290 (2018).

[34] S. Datta, *Electronic Transport in Mesoscopic Systems* (Cambridge University Press, Cambridge, 2007).

[35] H. Haug and A.-P. Jauho, *Quantum Kinetics in Transport and Optics of Semiconductors* (Springer, Berlin, 2010).

[36] H. Jiang, L. Wang, Q.-f. Sun, and X. C. Xie, Numerical study of the topological anderson insulator in HgTe/CdTe quantum wells, Phys. Rev. B **80**, 165316 (2009).

[37] Y. Zhang, J.-P. Hu, B. A. Bernevig, X. R. Wang, X. C. Xie, and W. M. Liu, Quantum blockade and loop currents in graphene with topological defects, Phys. Rev. B **78**, 155413 (2008).

[38] S. Nakanishi and M. Tsukada, Quantum Loop Current in a C_{60} Molecular Bridge, Phys. Rev. Lett. **87**, 126801 (2001).

[39] Y. Aharonov and D. Bohm, Significance of electromagnetic potentials in the quantum theory, Phys. Rev. **115**, 485 (1959).

[40] R. Schuster, E. Buks, M. Heiblum, D. Mahalu, V. Umansky, and H. Shtrikman, Phase measurement in a quantum dot via a double-slit interference experiment, Nature (London) **385**, 417 (1997).

[41] O. Klein, Die reflexion von elektronen an einem potentialsprung nach der relativistischen dynamik von Dirac, Z. Phys. **53**, 157 (1929).

[42] D. Li and J. Shi, Dorokhov-Mello-Pereyra-Kumar equation for the edge transport of a quantum spin Hall insulator, Phys. Rev. B **79**, 241303(R) (2009).

[43] C. L. Kane and E. J. Mele, Z_2 Topological Order and the Quantum Spin Hall Effect, Phys. Rev. Lett. **95**, 146802 (2005).

[44] A. Einstein and N. Rosen, The particle problem in the general theory of relativity, Phys. Rev. **48**, 73 (1935).

[45] H. Maier, J. Ziegler, R. Fischer, D. Kozlov, Z. D. Kvon, N. Mikhailov, S. A. Dvoretsky, and D. Weiss, Ballistic geometric resistance resonances in a single surface of a topological insulator, Nat. Commun. **8**, 2023 (2017).

[46] L. Du, S. Wang, D. Scarabelli, L. N. Pfeiffer, K. W. West, S. Fallahi, G. C. Gardner, M. J. Manfra, V. Pellegrini, S. J. Wind *et al.*, Emerging many-body effects in semiconductor artificial graphene with low disorder, Nat. Commun. **9**, 3299 (2018).

[47] C. Yang, Y. Liu, Y. Wang, L. Feng, Q. He, J. Sun, Y. Tang, C. Wu, J. Xiong, W. Zhang *et al.*, Intermediate bosonic metallic state in the superconductor-insulator transition, Science **366**, 1505 (2019).

[48] T. Ozawa, H. M. Price, A. Amo, N. Goldman, M. Hafezi, L. Lu, M. C. Rechtsman, D. Schuster, J. Simon, O. Zilberberg, and I. Carusotto, Topological photonics, Rev. Mod. Phys. **91**, 015006 (2019).

[49] L. Lu, J. D. Joannopoulos, and M. Soljačić, Topological photonics, Nat. Photonics **8**, 821 (2014).

[50] Y. Liu, X. Chen, and Y. Xu, Topological phononics: From fundamental models to real materials, Adv. Funct. Mater. **30**, 1904784 (2019).

[51] Z.-G. Chen and Y. Wu, Tunable Topological Phononic Crystals, Phys. Rev. Appl. **5**, 054021 (2016).

[52] X. Cai, L. Ye, C. Qiu, M. Xiao, R. Yu, M. Ke, and Z. Liu, Symmetry-enforced three-dimensional Dirac phononic crystals, Light: Sci. Appl. **9**, 38 (2020).

[53] J. Ningyuan, C. Owens, A. Sommer, D. Schuster, and J. Simon, Time- and Site-Resolved Dynamics in a Topological Circuit, Phys. Rev. X **5**, 021031 (2015).

[54] V. V. Albert, L. I. Glazman, and L. Jiang, Topological Properties of Linear Circuit Lattices, Phys. Rev. Lett. **114**, 173902 (2015).

[55] Y. Yang, Z. Gao, H. Xue, L. Zhang, M. He, Z. Yang, R. Singh, Y. Chong, B. Zhang, H. Chen *et al.*, Realization of a three-dimensional photonic topological insulator, Nature (London) **565**, 622 (2019).

[56] C. He, S.-Y. Yu, H. Wang, H. Ge, J. Ruan, H. Zhang, M.-H. Lu, and Y.-F. Chen, Hybrid Acoustic Topological Insulator in Three Dimensions, Phys. Rev. Lett. **123**, 195503 (2019).

[57] Z. Wang, Y. D. Chong, J. D. Joannopoulos, and M. Soljacic, Reflection-Free One-Way Edge Modes in a Gyromagnetic Photonic Crystal, Phys. Rev. Lett. **100**, 013905 (2008).

[58] Z. Wang, Y. Chong, J. D. Joannopoulos, and M. Soljačić, Observation of unidirectional backscattering-immune topological electromagnetic states, Nature (London) **461**, 772 (2009).

[59] X. Wen, C. Qiu, Y. Qi, L. Ye, M. Ke, F. Zhang, and Z. Liu, Acoustic Landau quantization and quantum-Hall-like edge states, Nat. Phys. **15**, 352 (2019).

[60] T. Hofmann, T. Helbig, C. H. Lee, M. Greiter, and R. Thomale, Chiral Voltage Propagation and Calibration in a Topolectrical Chern Circuit, Phys. Rev. Lett. **122**, 247702 (2019).

[61] L. Brey and H. A. Fertig, Electronic states of wires and slabs of topological insulators: Quantum Hall effects and edge transport, Phys. Rev. B **89**, 085305 (2014).

[62] S. B. D. Altland Alexander, *Condensed Matter Field Theory*, 2nd ed. (Cambridge University Press, Cambridge, 2010).